## PAPER

Check for updates

# Efficient second- and higher-order harmonic generation from LiNbO₃ metasurfaces

Yun Zhao,[a] Zhaoxi Chen,[b] Cheng Wang,*[b] Yuanmu Yang ![ID] *[a] and Hong-Bo Sun ![ID] *[a]

Lithium niobate (LiNbO₃) is a material that has drawn great interest in nonlinear optics because of its large nonlinear susceptibility and wide transparency window. However, for complex nonlinear processes such as high-harmonic generation (HHG), which involves frequency conversion over a wide frequency range, it can be extremely challenging for a bulk LiNbO₃ crystal to fulfill the phase-matching conditions. LiNbO₃ metasurfaces with resonantly enhanced nonlinear light–matter interaction at the nanoscale may circumvent such an issue. Here, we experimentally demonstrate efficient second-harmonic generation (SHG) and HHG from a LiNbO₃ metasurface enhanced by guided-mode resonance. We observe a high normalized SHG efficiency of $5.1 \times 10^{-5}$ cm² GW⁻¹. Moreover, with the alleviated above-gap absorption of the material, we demonstrate HHG up to the 7ᵗʰ order with the shortest generated wavelength of 226 nm. This work may provide a pathway towards compact coherent white-light sources with frequency spanning into the deep ultraviolet region for applications in spectroscopy and imaging.

## Introduction

Lithium niobate (LiNbO₃) is a widely used material for nonlinear optics. It is transparent over a broad spectral range from ultraviolet (UV) to mid-infrared. Due to the lack of centrosymmetry of its crystal structure, LiNbO₃ exhibits both even- and odd-order nonlinear responses. Most notably, the large second-order nonlinear susceptibility ($\chi^{(2)}$) allows it to be used for efficient second-order nonlinear optical processes such as second-harmonic generation (SHG),[1,2] sum- and difference-frequency generation,[3,4] and spontaneous parametric down-conversion (SPDC).[5,6] In addition, LiNbO₃ can also be appealing in third-order nonlinear interactions, including four-wave mixing[7] and Kerr-based optical frequency comb generation.[8,9]

To allow efficient nonlinear light–matter interaction in a bulk LiNbO₃ crystal or a LiNbO₃ waveguide, the phase-matching conditions must be met.[10] Nonetheless, conventional phase-matching techniques, including birefringent phase-matching and quasi-phase-matching, typically only work for a limited bandwidth and do not perform well for nonlinear processes such as high-harmonic generation (HHG), which involves frequency conversion over many octaves. To tackle

this challenge, it was recently shown that a stringently engineered chirped periodically poled LiNbO₃ (CPPLN) crystal can allow HHG up to the 10ᵗʰ order,[11–13] generating a supercontinuum white light source spanning an extremely wide wavelength range from 350 nm to 2500 nm. However, HHG into the deep ultraviolet (DUV) spectral range is yet to be observed due to the strong absorption of the above-gap harmonics when propagating inside such a bulk LiNbO₃ crystal.

The abovementioned issues of phase mismatch and above-gap absorption may be partly addressed using LiNbO₃ metasurfaces with a subwavelength thickness. With the rapid development of lithium niobate on insulator (LNOI)[14] technology over the last few years, LiNbO₃ thin films can now be patterned into metasurfaces[15] that support a variety of Mie resonances, including electric- or magnetic-dipole resonance,[16–18] Fano resonance,[19,20] anapole resonance,[21,22] bound states in the continuum (BIC) resonance,[23–27] and guided-mode resonance.[28–30] For SHG, LiNbO₃ metasurfaces with resonantly enhanced nonlinear light–matter interaction have been demonstrated, yet with relatively low conversion efficiency, which may be due to the relatively low $Q$-factors limited by design or fabrication constraints. For HHG, reports from LiNbO₃ metasurfaces remain elusive. HHG from the Si metasurface,[31,32] GaP metasurface,[33] and sub-wavelength-thick epsilon-near-zero thin film[34] has been demonstrated, yet the relatively strong above-gap absorption loss in the UV region still poses an issue.

In this work, we demonstrate efficient SHG and HHG up to the 7ᵗʰ order, with the shortest generated wavelength of 226 nm in the DUV regime, from a LiNbO₃ metasurface that

*[a] State Key Laboratory of Precision Measurement Technology and Instruments, Department of Precision Instrument, Tsinghua University, Beijing 100084, China. E-mail: ymyang@tsinghua.edu.cn, hbsun@tsinghua.edu.cn*
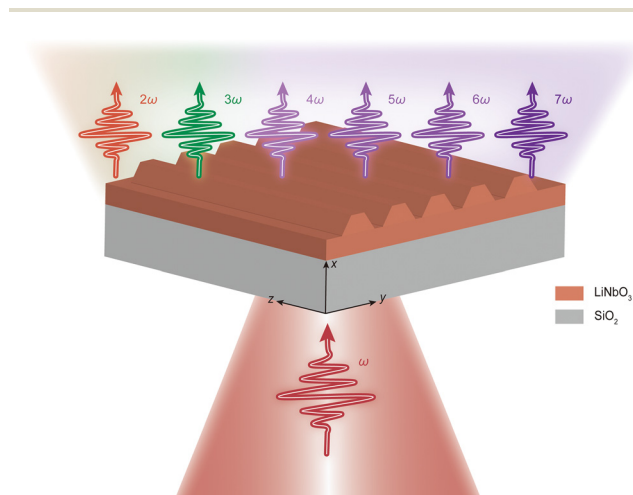
*[b] Department of Electronical Engineering and State Key Laboratory of Terahertz and Millimeter Waves, City University of Hong Kong, Hong Kong 999077, China. E-mail: cwang257@cityu.edu.hk*

supports a guided-mode resonance. When the metasurface is resonantly driven by a transverse electric (TE) polarized femtosecond laser, we observed a high SHG conversion efficiency of $8.6 \times 10^{-3}$ at a peak pump intensity of $0.17$ TW cm$^{-2}$. We further observed the $7^{th}$ harmonic generation in the DUV region.



**Fig. 1** Schematic of HHG from a LiNbO$_3$ metasurface supporting guided-mode resonance. When the TE-polarized pump laser is normally incident from the substrate side, the nonlinear harmonic signals from the $2^{nd}$ to $7^{th}$ order are emitted in the transmission direction. The metasurface is composed of a LiNbO$_3$ grating whose optical axis is along the $z$-direction situated on a SiO$_2$/quartz substrate.

# Results

The metasurface supporting guided-mode resonance, composed of a partially-etched 1D LiNbO$_3$ grating, is fabricated on an $x$-cut LNOI wafer. The wafer has a 600-nm-thick LiNbO$_3$ thin-film layer on a 2-μm-thick SiO$_2$ box layer placed on a 500-μm-thick transparent quartz substrate, and the schematic is shown in Fig. 1. The optical axis of the LiNbO$_3$ thin-film is along the $z$-direction and the pump laser is polarized along the TE direction to utilize LiNbO$_3$'s largest second-order nonlinear tensor component $d_{33}$. The harmonic signals from the $2^{nd}$ to $7^{th}$ order spanning the near-infrared to DUV wavelength range are generated in the transmission direction with a femtosecond pump laser incident in the normal direction.

Fig. 2a depicts the geometry of the grating which is designed to support high-$Q$ guided-mode resonance. We calculate the eigenmodes and the transmission spectrum of the metasurface for TE polarization using the commercial software Lumerical FDTD (see Numerical simulations in the Methods section for more details). The photonic band structure of the 1D subwavelength grating is shown in Fig. 2b, which reveals two strong resonances in the first Brillouin zone, corresponding to a guided-mode resonance and a BIC resonance, respectively. Though the BIC resonance can have an extremely large $Q$-factor approaching infinity, it is prohibited to couple with normally incident light due to symmetry constraints.[35] In contrast, the guided-mode resonance can be excited under



**Fig. 2** (a) Schematic illustration of a unit cell of the LiNbO$_3$ metasurface. The geometric parameters are $w$ = 260 nm, $h$ = 240 nm, $H$ = 600 nm, $p$ = 850 nm, and $\theta$ = 45°. (b) Calculated band structure of the LiNbO$_3$ metasurface. (c) Measured (red) and simulated (blue) transmittance spectra of the LiNbO$_3$ metasurface, respectively. (d) Simulated electric field distribution in the $x$–$y$ plane at a resonant wavelength of 1580 nm. The box illustrates the LiNbO$_3$ region. (e) An optical photo of the fabricated LiNbO$_3$ metasurface. (f) A representative SEM image of the fabricated LiNbO$_3$ metasurface.

Fig. 3 (a) Schematic of the nonlinear harmonic generation measurement setup. (b) The measured SHG spectrum of the LiNbO₃ metasurface with the pump wavelength varying from 1550 nm to 1630 nm at an interval of 10 nm. (c) Log–log plot of the SHG intensity as a function of the excitation intensity. The dots are the measured SHG intensity and the line is a numerical fit with a slope of 2.03. (d) The measured SHG spectrum of the LiNbO₃ metasurface (red) and an unpatterned film (blue), respectively, under TE polarization. (e) Measured SHG intensity as a function of the polarization angle of the pump laser beam.

normal incidence, occurring at a wavelength of 1580 nm. The simulated normal-incident transmittance spectrum of the metasurface, as shown in Fig. 2c, also indicates that only the guided-mode resonance is excited. The electric field distribution at the resonant wavelength is given in Fig. 2d, which shows about 9-fold enhancement of the local electric field confined inside the LiNbO₃ structure. The optical photo and scanning electron microscopy (SEM) images of the fabricated metasurface, patterned by electron beam lithography (EBL) followed by reactive ion etching (RIE), are shown in Fig. 2e and f (see Sample fabrication in the Methods section for more details). Subsequently, the linear transmittance spectrum of the fabricated metasurface is experimentally measured under TE-polarized normal incident light. As shown in Fig. 2c, the experimental result qualitatively agrees with the simulation. The lower extinction ratio and larger resonance linewidth may originate from the imperfection of fabrication as well as the finite angular range of the incident white light. To further experi-



Fig. 4 Comparison of SHG efficiency in Si, III−V semiconductors, and LiNbO₃ metasurfaces.

mentally characterize the nonlinear responses of the metasurface, we set up the nonlinear optical measurement system (see Optical characterization in the Methods section for more details) as schematically shown in Fig. 3a. The pump laser with a pulse duration of 290 fs and a repetition rate of 75 kHz is focused on the sample *via* a lens with a focal length of 50 mm. The polarization of the pump laser is controlled by a linear polarizer and a half-wave plate. The generated harmonic

signals are collected with a high numerical aperture lens (NA = 0.69) and then spatially dispersed with a $CaF_2$ prism before being coupled into the grating spectrometer.

By tuning the pump wavelength from 1550 nm to 1630 nm with a step of 10 nm at a constant peak pump intensity of 1.8 GW $cm^{-2}$, we observed a SHG signal peak at a pump wavelength of 1580 nm, as shown in Fig. 3b. The peak in the signal confirms the resonance enhancement of the SHG as a result of
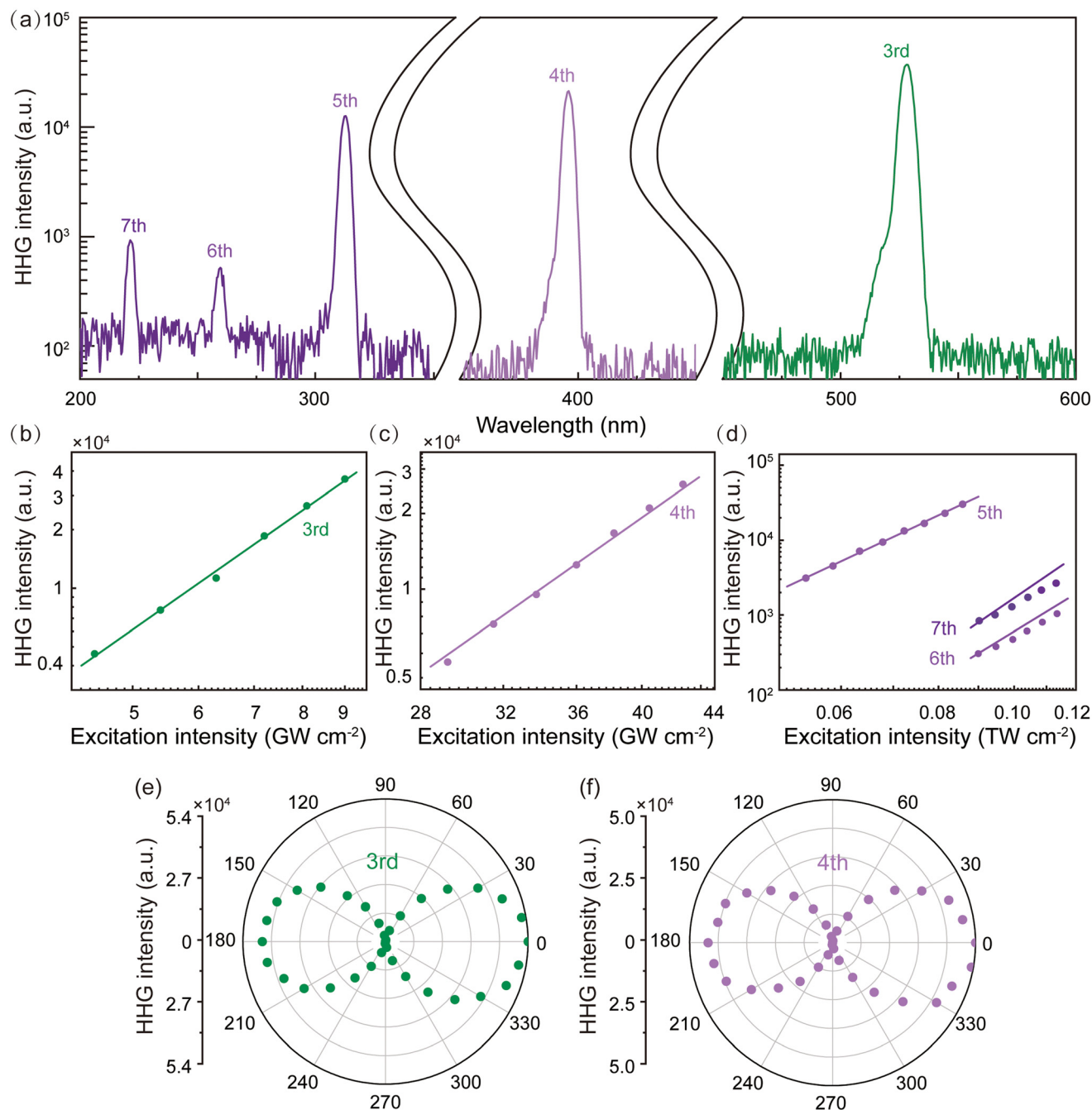


**Fig. 5** (a) Measured HHG spectrum of the $LiNbO_3$ metasurface. The plotted harmonic signals of the 3rd, 4th, and 5th–7th order are driven under a peak pump intensity of 9.04 GW $cm^{-2}$, 40.7 GW $cm^{-2}$, and 90.4 GW $cm^{-2}$, respectively. The black curved lines separate the harmonic spectra at different pump powers and integration times. (b–d) Log–log plot of the HHG intensity as a function of the excitation intensity. The dots are the measured $n$th harmonic intensity and the line scale as $I^n$. (e and f) Measured polarization states of the 3rd and 4th harmonics.

the guided-mode resonance. As the pump power increases, the SHG intensity exhibits a quadratic relationship with the excitation intensity, as depicted in Fig. 3c. The SHG intensity starts to drop at a peak pump intensity of 0.21 TW cm$^{-2}$, which corresponds to the damage threshold of the metasurface. Compared with an unpatterned LiNbO$_3$ film at an identical excitation intensity of 1.8 GW cm$^{-2}$, the SHG intensity of the LiNbO$_3$ metasurface is enhanced 7 times, as shown in Fig. 3d. Because of the polarization-sensitive nature of the GMR metasurface and the substantial difference in $\chi^{(2)}$ tensor components along the $z$- and $y$-crystal directions, the SHG intensity of LiNbO$_3$ gratings is strongly dependent on the polarization of the pump light, as shown in Fig. 3e. The intensity shows 80-fold enhancement in the resonant pump with TE polarization compared to the non-resonant pump with transverse magnetic (TM) polarization. At a peak pump intensity $I_{peak}^{FH}$ of 0.17 TW cm$^{-2}$, we measured a high absolute conversion efficiency $\eta = P_{avg}^{SH}/P_{avg}^{FH}$ of $8.6 \times 10^{-3}$, where $P_{avg}^{SH}$ is the average power of the second harmonic. Since the SHG efficiency is proportional to the peak pump intensity, we use the normalized SHG efficiency, defined as $\eta_{norm} = \eta/I_{peak}^{FH}$, as the criterion to benchmark the SHG efficiency of various metasurface platforms. The normalized efficiency of our LiNbO$_3$ metasurface is $5.1 \times 10^{-5}$ cm$^2$ GW$^{-1}$. We compare this value with other dielectric metasurfaces[36–41] including Si,[24,42,43] III–V semiconductors,[17,20,27,44–49] and other LiNbO$_3$ platforms[50–54] and summarize the results in Fig. 4. The high efficiency of our LiNbO$_3$ metasurface supporting guided-mode resonance may result from the large intrinsic second-order nonlinear coefficient of LiNbO$_3$ as well as the high $Q$-factor of the metasurface with fine fabrication process control and is comparable to some III–V semiconductor metasurfaces which have a larger second-order susceptibility.

Subsequently, we measured the higher-order nonlinear optical responses of the metasurface. As shown in Fig. 5a, harmonic signals from the 3$^{rd}$ to 7$^{th}$ order are observed when pumping the metasurface at a resonant wavelength of 1580 nm. Due to the non-centrosymmetric crystal structure of LiNbO$_3$, both even- and odd-order harmonics have been observed. Fig. 5b–d show the dependence of the $n^{th}$ harmonic intensity on the excitation intensity. The harmonic intensity of the 3$^{rd}$–5$^{th}$ order as $(I_{peak}^{FH})^{3,4,5}$, respectively, which indicates that the harmonic generations are in the perturbative regime. As the pump power increases further, the intensity of the 6$^{th}$ and 7$^{th}$ harmonics reaches the non-perturbative regime, which indicates that the strength of the laser field approaches the atomic bonding strength of the material.[55] We finally characterized the polarization states of the output even- and odd-order harmonics respectively when pumping with a TE-polarized beam at the resonant wavelength. As shown in Fig. 5e and f, both the 3$^{rd}$ and 4$^{th}$ harmonics have good linear polarizations with the same direction as the pump light which illustrates the dominant role of the nonlinear optical tensor $d_{33}$.

## Conclusions and discussion

Here, we experimentally demonstrate that using a LiNbO$_3$ metasurface supporting guided-mode resonance, one can achieve a normalized SHG conversion efficiency as high as $5.1 \times 10^{-5}$ cm$^2$ GW$^{-1}$ and HHG up to the 7$^{th}$ order, with the shortened wavelength down to 226 nm. Unlike bulk crystals that rely on the long propagation distance, nonlinear harmonic generation in LiNbO$_3$ metasurfaces with guided-mode resonance is not restricted by the phase-matching conditions. The LiNbO$_3$ metasurface is transparent over a wide spectral range, and thus may allow broadband THz generation,[56–58] SPDC,[59] and coherent supercontinuum white-light generation down to the DUV region. Furthermore, the metasurface may be tailored to have spatially varying amplitudes and phase responses at a subwavelength resolution,[60,61] thus enabling wavefront control for nonlinear harmonics of the LiNbO$_3$ metasurface.[62]

## Methods

### Numerical simulations

The simulation of the transmittance spectrum and electric field distribution of the metasurface is carried out using Lumerical FDTD. The periodic boundary conditions along the $y$-direction and PML boundary conditions along the $x$-direction are used. The light source which is a linearly polarized plane-wave pulse along the $z$-axis is normally incident from the substrate side. A field and power monitor is placed on the air side to calculate the transmittance. The photonic band structure of the metasurface for TE polarization is also calculated using Lumerical FDTD with Bloch boundary conditions along the $y$-direction and PML boundary conditions along the $x$-direction. A dipole cloud of 10 randomly positioned electric dipole sources is placed in each unit cell to excite the eigenmodes of TE polarization. An analysis group of 20 randomly positioned time monitors is used to calculate the band structure for an in-plane wave vector ranging from 0 to 0.1.

### Sample fabrication

To utilize the largest second-order susceptibility of LiNbO$_3$, an $x$-cut LNOI wafer is used whose crystallographic optical axis ($z$-axis) is located within the film plane. The fabrication of our device starts from an LNOI chip with a 600-nm-thick LiNbO$_3$ thin film, a 2-μm-thick SiO$_2$ buffer layer, and a 500-μm-thick quartz substrate. To fabricate the metasurface in the LiNbO$_3$ layer, a 150-nm-thick nichrome (NiCr) mask is first defined by EBL, thermal evaporation, and standard lift-off processes. The mask patterns are then transferred to the LiNbO$_3$ layer by standard RIE with argon (Ar$^+$)-based plasma. Finally, the residue of the NiCr mask is removed to reveal the metasurface array. The fabricated structure has a rib height of 240 nm, an unetched slab height of 360 nm, and a sidewall angle of ~45°. The entire footprint of each metasurface array is $200 \times 200$ μm$^2$.

### Optical characterization

For the measurement of the linear transmittance spectrum, white light emitted from a tungsten lamp is used as the light source. A linear polarizer and a half-wave plate are used to control the polarization of the incident light. Two pairs of dia-

phragms and lenses are used to achieve Köhler illumination conditions for the metasurface. The transmitted light is collected by an infrared objective (Mitutoyo, 50×, 0.42 NA) and then coupled to a camera-based grating spectrometer (Andor Kymera 328i and DU490A) through a multimode fiber.

For the nonlinear harmonic generation measurement, the excitation laser beam with a 290 fs pulse duration and a 75 kHz repetition rate is generated by an optical parametric amplifier (Light Conversion Orpheus-ONE-HP) pumped by a Yb: KGW laser amplifier (Light Conversion Pharos). A linear polarizer and a half-wave plate are used to adjust the polarization of the pump laser. The laser is focused onto the sample with a spot radius of 18 μm, using a lens with a focal length of 50 mm. The generated high-harmonic signals are collected by a high numerical aperture aspheric lens with an NA of 0.69 and further spatially dispersed by a $CaF_2$ prism (Thorlabs, PS863). The harmonic signals are finally coupled into a visible-UV grating spectrometer (Ideaoptics, PG2000-pro) for spectrum analysis through a multimode fiber.

## Author contributions

Yuanmu Yang proposed the project. Yun Zhao designed the sample and performed the simulation. Zhaoxi Chen fabricated the metasurface and Yun Zhao carried out the optical characterization. Yun Zhao and Yuanmu Yang prepared the manuscript. Cheng Wang, Yuanmu Yang, and Hong-Bo Sun supervised the research.

## Conflicts of interest

There are no conflicts to declare.

## Acknowledgements

## References

1 T. Sugita, K. Mizuuchi, Y. Kitaoka and K. Yamamoto, *Opt. Lett.*, 1999, **24**, 1590–1592.

2 N. Uesugi and T. Kimura, *Appl. Phys. Lett.*, 2008, **29**, 572–574.

3 D. Hofmann, G. Schreiber, C. Haase, H. Herrmann, W. Grundkötter, R. Ricken and W. Sohler, *Opt. Lett.*, 1999, **24**, 896–898.

4 W. Sohler and H. Suche, *Appl. Phys. Lett.*, 2008, **37**, 255–257.

5 S. Tanzilli, W. Tittel, H. De Riedmatten, H. Zbinden, P. Baldi, M. DeMicheli, D. B. Ostrowsky and N. Gisin, *Eur. Phys. J. D*, 2002, **18**, 155–160.

6 H. G. de Chatellus, A. V. Sergienko, B. E. A. Saleh, M. C. Teich and G. D. Giuseppe, *Opt. Express*, 2006, **14**, 10060–10072.

7 R. Normandin and G. I. Stegeman, *Opt. Lett.*, 1979, **4**, 58–59.

8 Y. He, Q.-F. Yang, J. Ling, R. Luo, H. Liang, M. Li, B. Shen, H. Wang, K. Vahala and Q. Lin, *Optica*, 2019, **6**, 1138–1144.

9 C. Wang, M. Zhang, M. Yu, R. Zhu, H. Hu and M. Loncar, *Nat. Commun.*, 2019, **10**, 978.

10 R. W. Boyd, *Nonlinear optics*, Academic press, 2020.

11 B.-Q. Chen, C. Zhang, C.-Y. Hu, R.-J. Liu and Z.-Y. Li, *Phys. Rev. Lett.*, 2015, **115**, 083902.

12 B. Chen, L. Hong, C. Hu and Z. Li, *Research*, 2021, **2021**, 1539730.

13 M. Li, L. Hong and Z.-Y. Li, *Research*, 2022, **2022**, 9871729.

14 P. Rabiei, J. Ma, S. Khan, J. Chiles and S. Fathpour, *Opt. Express*, 2013, **21**, 25573–25581.

15 G. Li, S. Zhang and T. Zentgraf, *Nat. Rev. Mater.*, 2017, **2**, 17010.

16 M. R. Shcherbakov, D. N. Neshev, B. Hopkins, A. S. Shorokhov, I. Staude, E. V. Melik-Gaykazyan, M. Decker, A. A. Ezhov, A. E. Miroshnichenko, I. Brener, A. A. Fedyanin and Y. S. Kivshar, *Nano Lett.*, 2014, **14**, 6488–6492.

17 S. Liu, M. B. Sinclair, S. Saravi, G. A. Keeler, Y. Yang, J. Reno, G. M. Peake, F. Setzpfandt, I. Staude, T. Pertsch and I. Brener, *Nano Lett.*, 2016, **16**, 5426.

18 H. Jiang, Y. Cai and Z. Han, *J. Opt. Soc. Am. B*, 2020, **37**, 3146–3151.

19 Y. Yang, W. Wang, A. Boulesbaa, I. I. Kravchenko, D. P. Briggs, A. Puretzky, D. Geohegan and J. Valentine, *Nano Lett.*, 2015, **15**, 7388–7393.

20 P. P. Vabishchevich, S. Liu, M. B. Sinclair, G. A. Keeler, G. M. Peake and I. Brener, *ACS Photonics*, 2018, **5**, 1685.

21 G. Grinblat, Y. Li, M. P. Nielsen, R. F. Oulton and S. A. Maier, *ACS Photonics*, 2017, **4**, 2144–2149.

22 M. Semmlinger, M. Zhang, M. L. Tseng, T.-T. Huang, J. Yang, D. P. Tsai, P. Nordlander and N. J. Halas, *Nano Lett.*, 2019, **19**, 8972–8978.

23 K. Koshelev, S. Lepeshov, M. Liu, A. Bogdanov and Y. Kivshar, *Phys. Rev. Lett.*, 2018, **121**, 193903.

24 Z. Liu, Y. Xu, Y. Lin, J. Xiang, T. Feng, Q. Cao, J. Li, S. Lan and J. Liu, *Phys. Rev. Lett.*, 2019, **123**, 253901.

25 K. Koshelev, Y. Tang, K. Li, D. Y. Choi, G. Li and Y. Kivshar, *ACS Photonics*, 2019, **6**, 1639.

26 A. P. Anthur, H. Zhang, R. Paniagua-Dominguez, D. A. Kalashnikov, S. T. Ha, T. W. W. Maß, A. I. Kuznetsov and L. Krivitsky, *Nano Lett.*, 2020, **20**, 8745–8751.

27 K. Koshelev, S. Kruk, E. Melik-Gaykazyan, J.-H. Choi, A. Bogdanov, H.-G. Park and Y. Kivshar, *Science*, 2020, **367**, 288–292.

28 S. Fan and J. D. Joannopoulos, *Phys. Rev. B: Condens. Matter Mater. Phys.*, 2002, **65**, 235112.

29  X. Gao, C. W. Hsu, B. Zhen, X. Lin, J. D. Joannopoulos, M. Soljačić and H. Chen, *Sci. Rep.*, 2016, **6**, 31908.

30  J. Jin, X. Yin, L. Ni, M. Soljačić, B. Zhen and C. Peng, *Nature*, 2019, **574**, 501–504.

31  H. Liu, C. Guo, G. Vampa, J. L. Zhang, T. Sarmiento, M. Xiao, P. H. Bucksbaum, J. Vučković, S. Fan and D. A. Reis, *Nat. Phys.*, 2018, **14**, 1006.

32  G. Zograf, K. Koshelev, A. Zalogina, V. Korolev, R. Hollinger, D.-Y. Choi, M. Zuerch, C. Spielmann, B. Luther-Davies, D. Kartashov, S. V. Makarov, S. S. Kruk and Y. Kivshar, *ACS Photonics*, 2022, **9**, 567–574.

33  M. R. Shcherbakov, H. Zhang, M. Tripepi, G. Sartorello, N. Talisa, A. AlShafey, Z. Fan, J. Twardowski, L. A. Krivitsky, A. I. Kuznetsov, E. Chowdhury and G. Shvets, *Nat. Commun.*, 2021, **12**, 4185.

34  Y. Yang, J. Lu, A. Manjavacas, T. S. Luk, H. Liu, K. Kelley, J.-P. Maria, E. L. Runnerstrom, M. B. Sinclair, S. Ghimire and I. Brener, *Nat. Phys.*, 2019, **15**, 1022–1026.

35  C. W. Hsu, B. Zhen, A. D. Stone, J. D. Joannopoulos and M. Soljačić, *Nat. Rev. Mater.*, 2016, **1**, 16048.

36  P. Vabishchevich and Y. Kivshar, *Photonics Res.*, 2023, **11**, B50–B64.

37  C. Gigli, G. Marino, A. Borne, P. Lalanne and G. Leo, *Front. Phys.*, 2019, **7**, 221.

38  D. Rocco, R. C. Morales, L. Xu, A. Zilli, V. Vinel, M. Finazzi, M. Celebrano, G. Leo, M. Rahmani, C. Jagadish, H. Tan, D. Neshev and C. De Angelis, *Adv. Phys.: X*, 2022, **7**, 2022992.

39  T. Liu, S. Xiao, B. Li, M. Gu, H. Luan and X. Fang, *Front. Nanotechnol.*, 2022, **4**, 891892.

40  G. Grinblat, *ACS Photonics*, 2021, **8**, 3406–3432.

41  K. Koshelev and Y. Kivshar, *ACS Photonics*, 2021, **8**, 102–112.

42  C. Fang, Q. Yang, Q. Yuan, L. Gu, X. Gan, Y. Shao, Y. Liu, G. Han and Y. Hao, *Laser Photonics Rev.*, 2022, **16**, 2100498.

43  Y. Zhao, W. Jia, X.-J. Wang, Y. Dong, H.-H. Fang, Y. Yang and H.-B. Sun, *Adv. Photonics Res.*, 2022, **3**, 2200157.

44  A. P. Anthur, H. Zhang, R. Paniagua-Dominguez, D. A. Kalashnikov, S. T. Ha, T. W. W. Maß, A. I. Kuznetsov and L. Krivitsky, *Nano Lett.*, 2020, **20**, 8745.

45  S. Liu, P. P. Vabishchevich, A. Vaskin, J. L. Reno, G. A. Keeler, M. B. Sinclair, I. Staude and I. Brener, *Nat. Commun.*, 2018, **9**, 2507.

46  L. Xu, G. Saerens, M. Timofeeva, D. A. Smirnova, I. Volkovskaya, M. Lysevych, R. Camacho-Morales, M. Cai, K. Z. Kamali, L. Huang, F. Karouta, H. H. Tan, C. Jagadish, A. E. Miroshnichenko, R. Grange, D. N. Neshev and M. Rahmani, *ACS Nano*, 2020, **14**, 1379–1389.

47  R. Camacho-Morales, M. Rahmani, S. Kruk, L. Wang, L. Xu, D. A. Smirnova, A. S. Solntsev, A. Miroshnichenko, H. H. Tan, F. Karouta, S. Naureen, K. Vora, L. Carletti, C. De Angelis, C. Jagadish, Y. S. Kivshar and D. N. Neshev, *Nano Lett.*, 2016, **16**, 7191–7197.

48  V. F. Gili, L. Carletti, A. Locatelli, D. Rocco, M. Finazzi, L. Ghirardini, I. Favero, C. Gomez, A. Lemaître, M. Celebrano, C. De Angelis and G. Leo, *Opt. Express*, 2016, **24**, 15965–15971.

49  S. S. Kruk, R. Camacho-Morales, L. Xu, M. Rahmani, D. A. Smirnova, L. Wang, H. H. Tan, C. Jagadish, D. N. Neshev and Y. S. Kivshar, *Nano Lett.*, 2017, **17**, 3914–3918.

50  Z. Huang, K. Luo, Z. Feng, Z. Zhang, Y. Li, W. Qiu, H. Guan, Y. Xu, X. Li and H. Lu, *Sci. China: Phys., Mech. Astron.*, 2022, **65**, 104211.

51  L. Qu, L. Bai, C. Jin, Q. Liu, W. Wu, B. Gao, J. Li, W. Cai, M. Ren and J. Xu, *Nano Lett.*, 2022, **22**, 9652–9657.

52  A. Fedotova, M. Younesi, J. Sautter, A. Vaskin, F. J. F. Löchner, M. Steinert, R. Geiss, T. Pertsch, I. Staude and F. Setzpfandt, *Nano Lett.*, 2020, **20**, 8608.

53  J. Ma, F. Xie, W. Chen, J. Chen, W. Wu, W. Liu, Y. Chen, W. Cai, M. Ren and J. Xu, *Laser Photonics Rev.*, 2021, **15**, 2000521.

54  S. Yuan, Y. Wu, Z. Dang, C. Zeng, X. Qi, G. Guo, X. Ren and J. Xia, *Phys. Rev. Lett.*, 2021, **127**, 153901.

55  S. Ghimire and D. A. Reis, *Nat. Phys.*, 2019, **15**, 10–16.

56  L. Luo, I. Chatzakis, J. Wang, F. B. P. Niesler, M. Wegener, T. Koschny and C. M. Soukoulis, *Nat. Commun.*, 2014, **5**, 3055.

57  S. Keren-Zur, M. Tal, S. Fleischer, D. M. Mittleman and T. Ellenbogen, *Nat. Commun.*, 2019, **10**, 1778.

58  Y. Tu, X. Sun, H. Wu, X. Zan, Y. Yang, N. Liu, X. Wang, C. Meng, Z. Lyu, Z. Zhu, K. Liu, D. Zhang and Z. Zhao, *Front. Phys.*, 2022, **10**, 883703.

59  G. Marino, A. S. Solntsev, L. Xu, V. F. Gili, L. Carletti, A. N. Poddubny, M. Rahmani, D. A. Smirnova, H. Chen, A. Lemaître, G. Zhang, A. V. Zayats, C. De Angelis, G. Leo, A. A. Sukhorukov and D. N. Neshev, *Optica*, 2019, **6**, 1416–1422.

60  L. Huang, X. Chen, H. Mühlenbernd, G. Li, B. Bai, Q. Tan, G. Jin, T. Zentgraf and S. Zhang, *Nano Lett.*, 2012, **12**, 5750–5755.

61  G. Li, S. Chen, N. Pholchai, B. Reineke, P. W. H. Wong, E. Y. B. Pun, K. W. Cheah, T. Zentgraf and S. Zhang, *Nat. Mater.*, 2015, **14**, 607–612.

62  M. Sivis, M. Taucer, G. Vampa, K. Johnston, A. Staudte, A. Y. Naumov, D. M. Villeneuve, C. Ropers and P. B. Corkum, *Science*, 2017, **357**, 303–306.